

# High-Precision Multibit Opto-Electronic Synapses Based on ReS<sub>2</sub>/h-BN/Graphene Heterostructure for Energy-Efficient and High-Accuracy Neuromorphic Computing

Zheyu Yang, Shida Huo, Zhe Zhang, Fanying Meng, Baiyan Liu, Yue Wang, Yuexuan Ma, Zhiyuan Wang, Junxi Xu, Qijia Tian, Yaohui Wang, Yingxuan Ding, Xiaodong Hu, Yuan Xie,\* Shuangqing Fan,\* Caofeng Pan,\* and Enxiu Wu\*

Neuromorphic computing integrates sensing, memory, and computation to surpass the von Neumann bottleneck. Opto-electronic synapses, capable of handling both optical and electrical signals, closely emulate biological synapses and enable advanced neuromorphic functionalities. Among them, optoelectronic floating-gate transistors (OEFGTs) based on 2D van der Waals (vdW) heterostructures offer high bandwidth, minimal crosstalk, and multilevel data storage. However, improving optical synaptic weights remains crucial for enhancing learning efficiency and reducing power consumption. In this study, an OEFGT-based opto-electronic synapse using a rhenium disulfide/hexagonal boron nitride/graphene (ReS<sub>2</sub>/h-BN/Gra) vdW heterostructure is demonstrated. This device achieves unprecedented high-precision multibit optical synaptic weights, reaching 1024 discrete levels (10-bit resolution)—the highest reported for 2D-material-based OEFGTs. Consequently, it realizes ultra-low energy consumption (500 fJ/spike) and various synaptic behaviors, including electrical and optical paired-pulse facilitation, depression, and spike-timing-dependent plasticity. Furthermore, the device successfully mimics classical conditioning (Pavlov's dog experiment), and primate associative learning, and performs reconfigurable logic operations ("AND", "OR", and "NIMP"). An optoelectronic neural network incorporating this synapse achieved 98.8% accuracy after 200 epochs in a color vision recognition task. This work highlights significant potential for OEFGT-based optoelectronic synapses with multibit optical weights in energy-efficient, high-performance neuromorphic computing.

## 1. Introduction

Neuromorphic computing (NC) is inspired by the information processing and transmission mechanisms of biological neural structures.<sup>[1,2]</sup> By integrating sensing, memory, and computation at the hardware level, NC aims to alleviate the von Neumann bottleneck caused by the physical separation of memory and the central processing unit.<sup>[3–6]</sup> The fundamental unit of biological neural structures is the synapse; thus, the development of artificial synaptic devices is essential for realizing NC. These devices emulate biological synapses through functionalities such as synaptic weight modulation, information encoding and decoding, and pattern recognition.<sup>[1,7–15]</sup>

Extensive research has explored various artificial synapses, including all-electrical synapses,<sup>[7–9]</sup> all-optical synapses,<sup>[1,10,11]</sup> and optoelectronic synapses.<sup>[12–15]</sup> Among these, opto-electronic synapses most closely resemble the hybrid signal processing mechanism of biological synapses, enabling complex functions such as associative learning and opto-electronic neural computing.<sup>[1,7–11]</sup> Opto-electronic

Z. Yang, S. Huo, Z. Zhang, F. Meng, B. Liu, Y. Wang, Y. Ma, Z. Wang, J. Xu, Q. Tian, Y. Wang, Y. Ding, X. Hu, E. Wu  
State Key Laboratory of Precision Measurement Technology and Instruments, School of Precision Instruments and Opto-electronics Engineering  
Tianjin University  
Tianjin 300072, P. R. China  
E-mail: [enxiuwu@tju.edu.cn](mailto:enxiuwu@tju.edu.cn)

Z. Yang, C. Pan  
Institute of Atomic Manufacturing  
Beihang University  
Beijing 100191, P. R. China  
E-mail: [pancaofeng@buaa.edu.cn](mailto:pancaofeng@buaa.edu.cn)

 The ORCID identification number(s) for the author(s) of this article can be found under <https://doi.org/10.1002/adfm.202509119>

DOI: 10.1002/adfm.202509119

Y. Xie  
School of Electronics and Information Engineering  
Tiangong University  
Tianjin 300387, P. R. China  
E-mail: [xieyuan@tiangong.edu.cn](mailto:xieyuan@tiangong.edu.cn)

Y. Xie  
Laboratory of Solid State Microstructures  
Nanjing University  
Nanjing 210093, P. R. China

S. Fan  
College of Electronics & Information  
Qingdao University  
Qingdao 266071, P. R. China  
E-mail: [sqfan@qdu.edu.cn](mailto:sqfan@qdu.edu.cn)

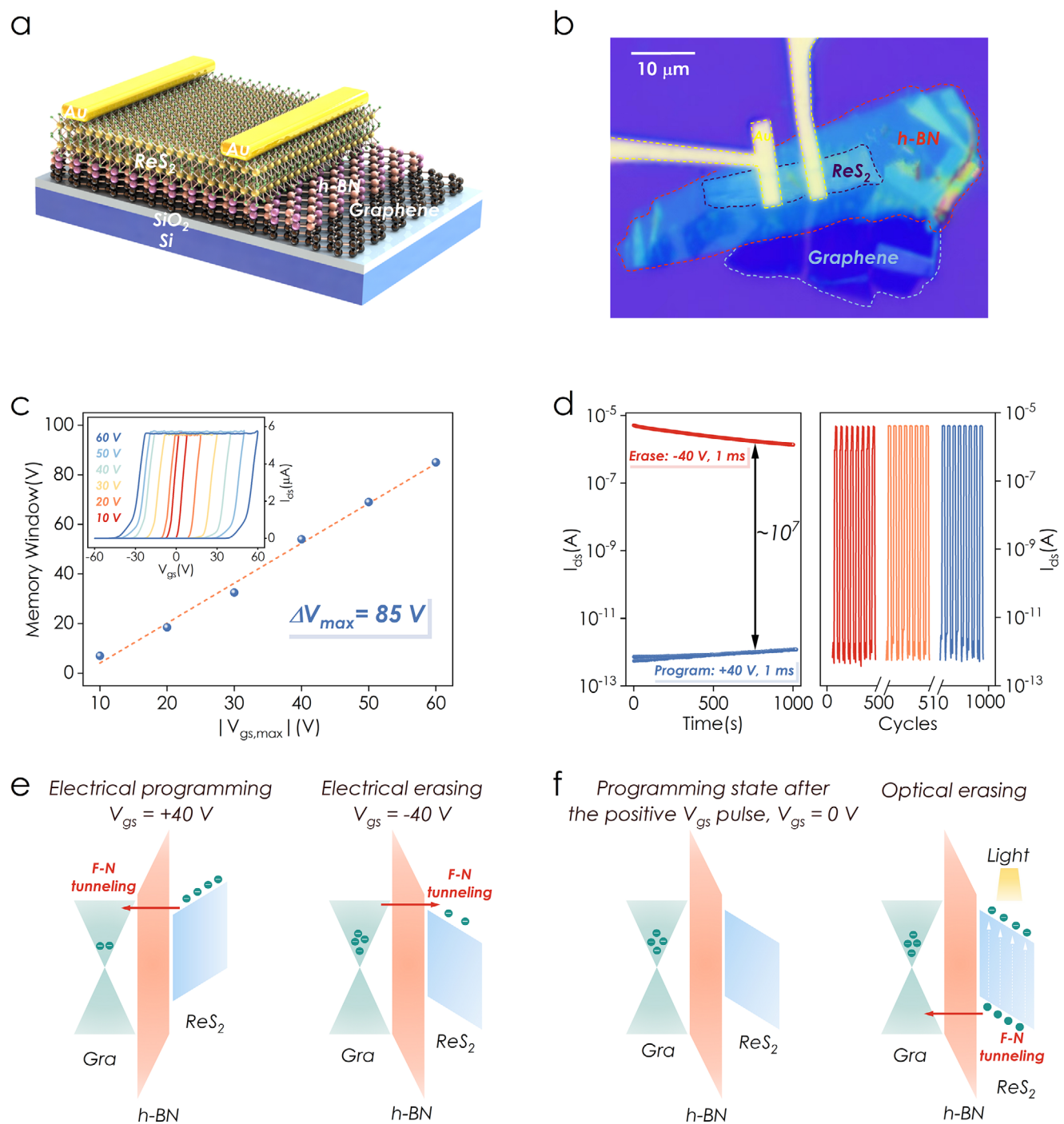


**Figure 1.** Device structure, memory performance and memory mechanism. Schematic illustration a) and optical microscopy b) of the ReS<sub>2</sub>/h-BN/Gra heterostructure. c) Memory window as a function of the maximum value of the V<sub>gs</sub> (V<sub>gs,max</sub>). Inset is the transfer characteristic curves under different V<sub>gs</sub> scan ranges. d) Retention characteristic and the endurance performance of the nonvolatile memory after applying a ±40 V, 1 ms pulse. e) Schematic of the energy bands during electrical programming and erasing. f) Schematic of the energy bands during optical erasing.

floating-gate transistors (OEFGTs) have emerged as promising candidates for opto-electronic synapses,<sup>[16–19]</sup> due to their high bandwidth, low crosstalk, and multilevel storage capability.

2D materials, characterized by atomic thickness, dangling bond-free surfaces, and high carrier mobility, effectively miti-

gate the short-channel effects of silicon-based transistors.<sup>[20,21]</sup> Their electronic transport properties can also be precisely controlled via external fields and van der Waals (vdW) heterogeneous integration,<sup>[20,22–24]</sup> making them ideal for OEFGT-based optoelectronic synapses. Various studies have reported OEFGTs



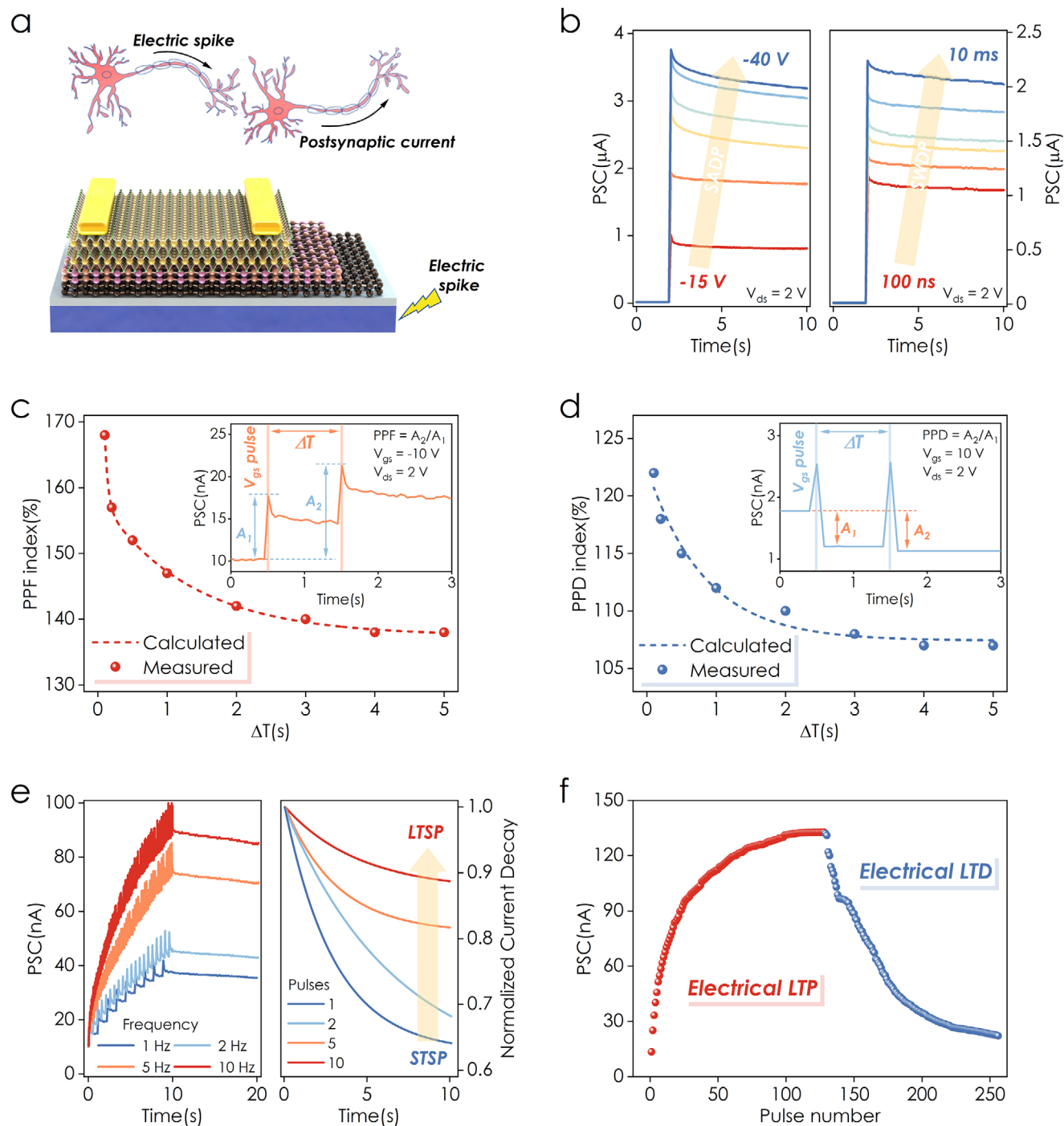


**Figure 2.** Synaptic plasticity of electrical synapse. a) Schematic illustration of a synapse transistor driven by electrical spikes. b) PSC as voltage amplitudes vary from  $-15$  to  $-40$  V (1 ms), corresponding to SADP. PSC as pulse widths range from 100 ns to 10 ms ( $-20$  V), corresponding to SWDP. c) Functional relationship between the PPF index and  $\Delta T$ . Inset is input  $V_{gs}$  pulses ( $10$  V, 1 ms) and current responses for PPF. d) Functional relationship between the PPD index and  $\Delta T$ . Inset is input  $V_{gs}$  pulses ( $10$  V, 1 ms) and current responses for PPD. e) PSC as pulse numbers increase from 1 to 10 within 10 s, corresponding to SFDP ( $-10$  V, 1 ms). PSC with an increasing number of voltage pulses from 1 to 10, corresponding to SNDP ( $-10$  V, 1 ms, 1 Hz). f) Process of electrical LTP and electrical LTD through electrical programming and erasing. Programming pulses:  $-4.5$  V, 10 ms, 1 Hz; erasing pulses: 9 V, 10 ms, 1 Hz.

altering the characteristic parameters of the voltage pulses, including spike amplitude-dependent plasticity (SADP), spike width-dependent plasticity (SWDP), spike number-dependent plasticity (SNDP), and spike frequency-dependent plasticity (SFDP). As illustrated in Figure 2b, negative electrical spikes with varying amplitudes (−15 to −40 V, 1 ms) and widths (−20 V, 100 ns to 10 ms) were applied to the synapse device. With increasing amplitude and width, more electrons are released into the channel, resulting in enhanced excitatory PSCs. Similarly, when positive pulses of different amplitudes and widths are applied, inhibitory PSCs decrease with the widening and heightening of the positive spikes (Figure S4, Supporting Information).

Subsequently, by applying two consecutive  $V_{gs}$  pulses (−10 and 10 V) with a width of 1 ms, two distinct forms of short-term synaptic plasticity (STSP), namely paired-pulse facilitation (PPF) and paired-pulse depression (PPD), were demonstrated. The PSC changes evoked by the two spikes are represented by  $A_1$  and  $A_2$ , thus allowing the calculation of PPF (PPD) index as  $A_2/A_1$ . The PPF and PPD behaviors are strongly correlated with the time interval ( $\Delta T$ ) of two consecutive  $V_{gs}$  pulses and the relaxation time ( $\tau$ ) of the tunneling electrons. They exhibit a typical biphasic exponential behavior, which can be fitted to a bi-exponential equation as follows:<sup>[28]</sup>

$$\text{PPF (PPD)} = C_1 \exp\left(-\frac{\Delta T}{\tau_1}\right) + C_2 \exp\left(-\frac{\Delta T}{\tau_2}\right) \quad (1)$$

where  $C_1$  and  $C_2$  are the initial enhancement amplitudes for fast and slow decay, respectively;  $\tau_1$  and  $\tau_2$  are the corresponding relaxation times. As shown in Figure 2c,d, the PPF and PPD index exhibit a monotonous decrease with  $\Delta T$ . For electrical synapses, the PPF index decreases from 168% to 138%, accompanied by  $\tau_1 = 0.05$  s and  $\tau_2 = 1.29$  s; Similarly, the PPD index decreases from 122% to 107%, with  $\tau_1 = 0.09$  s and  $\tau_2 = 1.55$  s. This suggests that the synaptic potentiation process exhibits a broader dynamic range, which is advantageous for more refined biomimetic learning. On the other hand, the extended relaxation time during the synaptic depression process may provide an advantage in the simulation of long-term plasticity.

Long-term synaptic plasticity (LTSP) is crucial for the adaptation, learning, and recovery of the nervous system. The exponential decay of the PPF index suggests that reducing the interval time of presynaptic spikes may effectively enhance synaptic connections. As shown in the left plot of Figure 2e, after 10 s of synaptic potentiation and 10 s of relaxation, the PSC gradually decays and stabilizes at a specific value. As the pulse (−10 V, 1 ms) frequency increases from 1 to 10 Hz, the final output current increases from 35 to 85 nA. Similar to the process of memory consolidation in the brain, the transition from STSP to LTSP can be achieved by repeatedly applying presynaptic spikes. The device was subjected to a different number of pulses (from 1 to 10) with the same amplitude, width, and frequency (−10 V, 1 ms, 1 Hz), and the PSC was recorded immediately after the pulses were removed. The fitting curve of the normalized current decay is shown in the right plot of Figure 2e. The synaptic weight quickly drops to 64% of the initial state after one pulse. When the number of applied pulses increases to 10, the synaptic weight stabilizes at 89%. In artificial neural networks, the number of synaptic weights is crucial for pattern recognition accuracy.<sup>[25,29]</sup> By ap-

plying repeated programming (−4.5 V, 10 ms, 1 Hz) and erasing (9 V, 10 ms, 1 Hz) pulses, long-term potentiation (LTP) and long-term depression (LTD) were induced. During electrical LTP and electrical LTD processes, the number of synaptic weights reached 128 (seven bits), as shown in Figure 2f.

### 2.3. Synaptic Plasticity of Opto-Electronic Synapses

In addition to the axon-dendrite structure excited by electrical spikes, light spikes can directly activate the axon-axon signaling pathway at the postsynaptic end (Figure 3a). The artificial synapse can recognize optical signals within a wavelength range from 255 to 638 nm, with consistent intensity and duration (100 mW cm<sup>−2</sup>, 1 s) for all signals (Figure S5, Supporting Information). To achieve the highest current spikes within the visible light spectrum, a 405 nm laser was employed to stimulate artificial synapses in subsequent experimental sections. Figure 3b presents a thermogram of  $I_{ds}$  correlated with light intensity and pulse width. Evidently, light spikes with greater power and width trigger an enhanced charge tunneling effect and excitatory PSCs. In biological visual systems, the PPF mechanism of optical synapses can enhance neuronal synchrony and improve of image processing efficiency.<sup>[25,29]</sup> Figure 3c demonstrates the PPF behavior achieved by applying two light pulses with identical intensity (100 mW cm<sup>−2</sup>) and width (1 s). The PPF index decreases from 153% to 136%, with  $\tau_1 = 0.17$  s and  $\tau_2 = 1.61$  s. Furthermore, by increasing the number and frequency of light pulses, the optical synapse transitions from STSP to LTSP (Figure S6, Supporting Information).

In the weight update process of the optoelectronic synapse, continuous light (1 mW cm<sup>−2</sup>, 10 ms, 1 Hz) and positive voltage (4.5 V, 10 ms, 1 Hz) pulses were used as excitation signals, as illustrated in Figure 3d. During the optical LTP process, the number of synaptic weights reached 1024 (10 bits), nearly an order of magnitude higher than that of the electrical LTP process. The multilevel conductance states of the optical synapse offer a computational paradigm closer to the biological brain, facilitating the development of more efficient and intelligent biomimetic visual neural networks. Additionally, the energy consumption per operation is 50 pJ/spike and 500 fJ/spike in the electrical and optical modes, respectively (Figure S7, Supporting Information). Optical programming exhibits lower energy consumption compared to electronic programming, attributed to the combined effect of the stored charge in the floating gate and optical input from the channel, which creates a lower tunneling barrier for photo-generated holes. Consequently, the minimum value unit of tunneling charge can be precisely compressed by controlling the power, duration, and frequency of optical pulses. Moreover, multilayer graphene, used as a floating gate to trap charge, expands the dynamic tuning range of synaptic weights. The enhancement in dynamic range and resolution is the direct cause of achieving storage levels of 10 bits. To benchmark our findings, Figure 3e compares the energy consumption and storage density of other optoelectronic synapses.<sup>[12,13,15,30–38]</sup> Our synaptic unit demonstrates persistent, robust, and energy-efficient storage operations, particularly offering a number of synaptic weights ten times higher than those reported for state-of-the-art devices in the literature.<sup>[12,13,15,30–38]</sup>

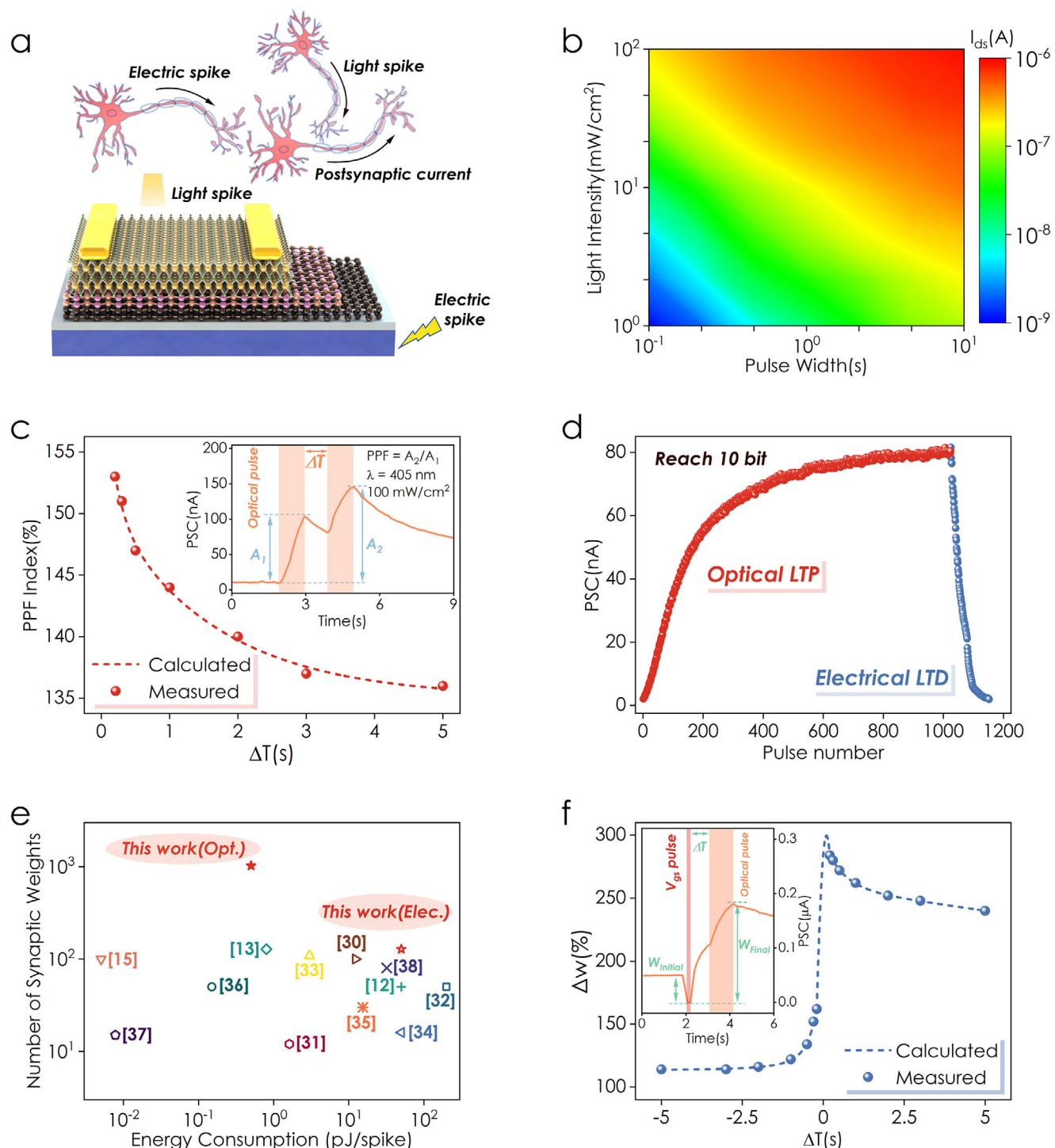


**Figure 3.** Synaptic plasticity of opto-electronic synapse. a) Schematic illustration of a synapse transistor modulated by light spikes. b) Thermal map of the  $I_{ds}$  as a function of optical power intensity and pulse width. c) Relationship between the optical PPF index and  $\Delta T$ . Inset is the input signal for optical PPF and its corresponding response (100 mW cm<sup>-2</sup>, 1 s). d) The process of optical LTP and electrical LTD. Programming pulses: 1 mW cm<sup>-2</sup>, 10 ms, 1 Hz; erasing pulses: 9 V, 10 ms, 1 Hz. e) Comparison of the proposed OEFGT based on ReS<sub>2</sub>/h-BN/Gra heterostructure with previously reported synaptic devices on energy consumption and storage density. f) Relationship between  $\Delta W$  and  $\Delta T$  in STDP. Inset is the input signal (voltage: -10 V, 1 ms, light: 1 mW cm<sup>-2</sup>, 1 s) for STDP and its PSC response.

Furthermore, we explored spike-timing-dependent plasticity (STDP), which is a learning rule that modifies the strength of connections between neurons based on the order of their spike signals.<sup>[39]</sup> In the canonical STDP mechanism, if the presynaptic neuron fires before the postsynaptic neuron, the synaptic connection is potentiated; conversely, if the postsynaptic neuron fires first, the connection is depressed. It enables neural networks to adapt to dynamic environments by dynamically adjusting the strength of synaptic connections. Through optoelectronic coupling at the presynaptic and postsynaptic terminals, the OEFGT based on ReS<sub>2</sub>/h-BN/Gra heterostructure successfully mimics the classical STDP. As shown in the inset of Figure 3f, updating the synaptic weight requires modifying the  $\Delta T$  between the presynaptic voltage pulse (-10 V, 1 ms) and the postsynaptic light pulse (1 mW cm<sup>-2</sup>, 1 s). When  $\Delta T > 0$ , the electrical spike precedes the optical spike; conversely, when  $\Delta T < 0$ , the optical spike is triggered first. The relative change in synaptic weight ( $\Delta W$ ) is calculated using the following equation:<sup>[40]</sup>

$$\Delta W = \frac{W_{\text{Final}} - W_{\text{Initial}}}{W_{\text{Initial}}} \quad (2)$$

where  $W_{\text{Initial}}$  represents the initial synaptic weight and  $W_{\text{Final}}$  is the final synaptic weight after two pulses. Figure 3f illustrates the dependence of  $\Delta W$  on  $\Delta T$  for the synaptic device. This STDP rule can be fit by the following equation:<sup>[40]</sup>

$$\Delta W = \begin{cases} A_1 \exp\left(-\frac{\Delta T}{t_1}\right) + A_{01} & (\Delta T < 0) \\ A_2 \exp\left(-\frac{\Delta T}{t_2}\right) + A_{02} & (\Delta T > 0) \end{cases} \quad (3)$$

where  $A_1$  and  $A_2$  are scaling factors,  $t_1$  and  $t_2$  are time constants, and  $A_{01}$  and  $A_{02}$  are constants. Based on the STDP fitting results,  $t_1$  and  $t_2$  are determined to be 0.37 and 1.27 s, respectively. The Hebbian learning rule,<sup>[39]</sup> a fundamental model for weight adjustment, provides the theoretical foundation for establishing neural network models. The STDP fitting curve closely aligns with the classical Hebbian rule, while its asymmetry potentially facilitates complex functions such as nonlinear mapping and pattern separation.<sup>[39]</sup> The asymmetry in the sequence of output current and input pulses suggests that the underlying mechanisms for triggering excitatory responses are distinct for the two types of signals. This discrepancy is likely due to the gate modulation effect during the electrical pulse.

#### 2.4. Complex Associative Learning and Reconfigurable Logic Functions

Paired associate learning in monkey brains represents a complex form of associative learning, forming neural connections between different brain regions to trigger cognitive responses to specific stimuli. In paired-associate tasks, an association is formed between two unrelated objects through the repeated pairing of a target item (e.g., color) with a specific stimulus (e.g., fruit). By utilizing the optoelectronic coupling of the OEFGT, we successfully established a pairing relationship between two colors and two fruits. Output currents below 200 nA and above

300 nA represented ineffective responses and pain perception, respectively. The pairing relationship was successfully established when the output current was between 200 and 300 nA. The experiment used electrical pulse sequences (1 ms, 1 Hz, 10 pulses) and optical pulse sequences (405 nm, 0.5 s, 1 Hz, 10 pulses) to simulate fruits and colors. Electrical pulses with amplitudes of -10 and -5 V represented banana and grape, denoted as signals 1 and 2, while optical pulses with power densities of 0.2 and 2 mW cm<sup>-2</sup> were used for yellow and purple cards, denoted as signals 1' and 2' (Figure 4a).

A single input of signals 1 and 1' demonstrated an ineffective pairing. After 5 training epochs, the association between the banana and the yellow card was successfully established. However, pairing signal 1 with 2' led to a significant pain response (Figure 4b). Similarly, the pairing task for signal 2 with 2' was successful, while pairing signal 2 with 1' resulted in failure (Figure 4c). These results suggest that the decay and forgetting of associative memory are governed by the spontaneous relaxation of photo-generated electrons. While the establishment and re-establishment of conditioned reflexes are linked to the excitation of these electrons.

Conditioned reflex, a form of associative learning, allows the brain to predict environmental changes and generate adaptive responses. The classically conditioned reflex experiment, particularly Pavlov's dogs,<sup>[41]</sup> demonstrates this process. In the experiment, a neutral stimulus (e.g., a bell sound) becomes capable of eliciting a conditioned reflex through its pairing with an unconditioned stimulus (e.g., food). Under the optoelectronic hybrid modulation mode, the OEFGT successfully simulates an extended version of Pavlov's experiment, including the establishment, extinction, re-establishment, and forgetting of conditioned reflexes. An output current of 100 nA was selected as the threshold for salivation. Voltage pulses (-10 V, 1 ms) served as the bell sound to trigger the conditioned reflex, while light pulses (405 nm, 2 mW cm<sup>-2</sup>, 0.5 s) mimicked the food stimulus inducing salivation, as shown in Figure 4a. Prior to training, 10 voltage pulses resulted in a PSC of 80 nA, insufficient to induce salivation. However, 10 light pulses increased the PSC to 240 nA, well above the threshold. During the training process, 10 synchronized voltage and light pulses established an association between the bell sound and food. After training, electrical stimulation alone increased the PSC to 130 nA, demonstrating the establishment of a conditioned reflex to the bell sound (Figure 4d). Following a 100-s rest, the same electrical stimulation no longer elicited salivation, indicating the extinction of the conditioned reflex. Due to residual photo-generated electrons in the channel, the conditioned reflex could be re-established with fewer retraining cycles. After five retraining cycles, electrical stimulation increased the PSC to 120 nA (Figure 4e). After an additional 500-s rest, the association between the bell and food was completely forgotten. As the device's conductivity fully recovered to its initial state, the bell sound stimulation after five retraining cycles failed to induce salivation (Figure 4f). These simulation experiments of paired associate learning and Pavlov's dogs indicate that the OEFGT based on ReS<sub>2</sub>/h-BN/Gra heterostructure can serve as a fundamental component for brain-like computing systems.

In addition to neuromorphic sensing, memory, and processing capabilities, dynamically reconfigurable logic operations can be achieved through optoelectronic synergy at dual-input terminals.

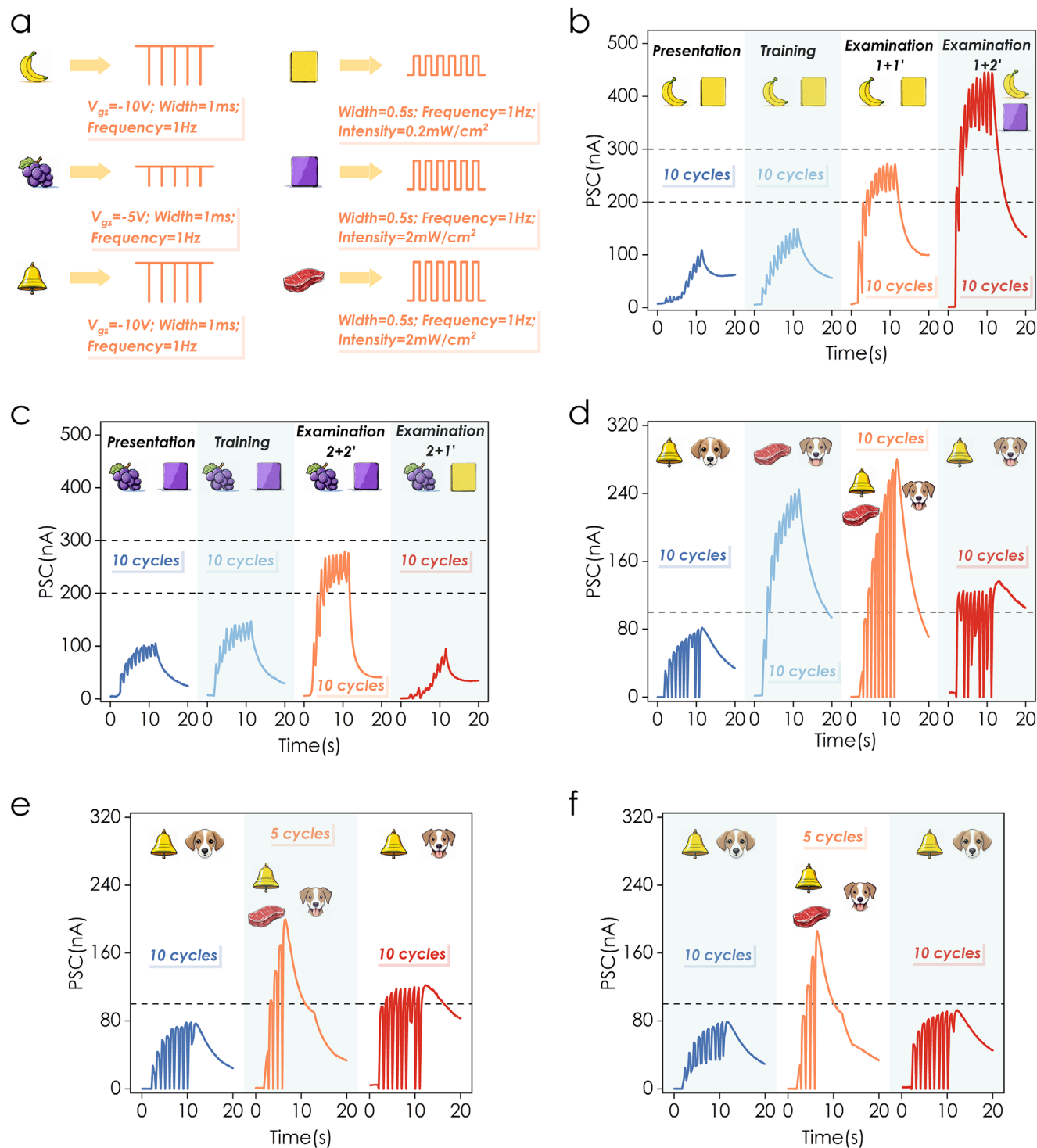


**Figure 4.** Paired associate learning in a monkey brain and extended experiment on Pavlov's dog. a) Correlation between  $V_{gs}$ /optical pulses and the banana/yellow card/grape/purple card/bell/food stimuli. b) Successful pairing of bananas and yellow in the test phase. Ineffective response to the pairing of bananas and purple. c) Successful pairing of grapes and purple in the test phase. Ineffective response to the pairing of grapes and yellow. d) Establishment of the conditioned reflex. e) Extinction of the conditioned reflex. f) Complete forgetting of the conditioned reflex.

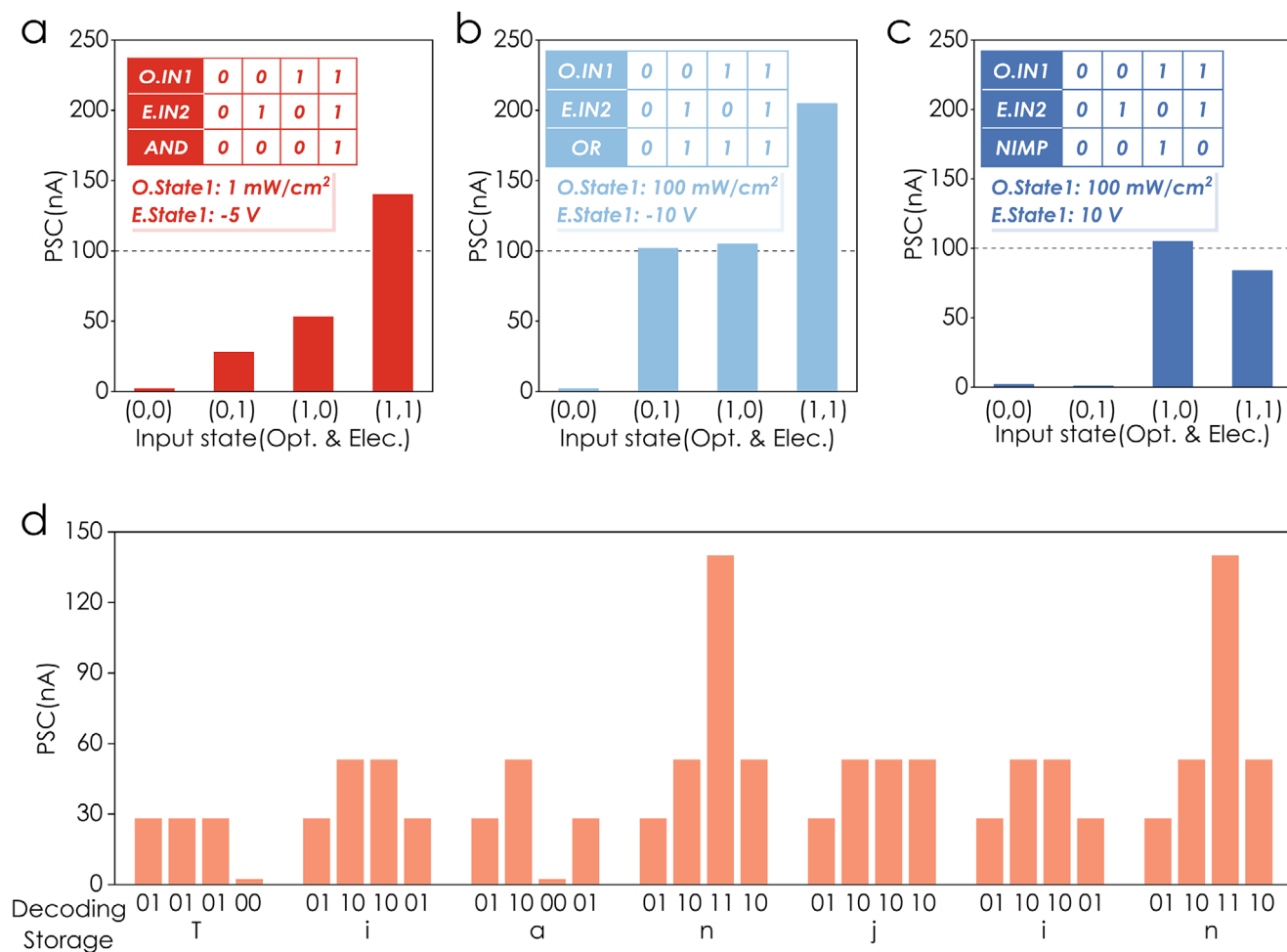


**Figure 5.** Reconfigurable logic gates with optical and electrical inputs. a) Readout current for the “AND” operation. b) Readout current for the “OR” operation. c) Readout current for the “NIMP” operation. d) Decoding process of the current information based on ASCII rules.

The output current is determined by the combined power density of the light pulse and the amplitude of the  $V_{gs}$  pulse. By selecting an appropriate threshold current, the device can perform various logic functions using both optical (1 s pulse width) and electrical (10 ms pulse width) input signals. For the “AND” operation, the input signals consist of a 1 mW cm<sup>-2</sup> light pulse and a -5 V  $V_{gs}$  pulse. For the “OR” operation, the input signals are a 100 mW cm<sup>-2</sup> light pulse and a -10 V  $V_{gs}$  pulse. For the “NIMP” operation, the input signals include a 100 mW cm<sup>-2</sup> light pulse and a 10 V  $V_{gs}$  pulse. The “0” and “1” states of the input signals correspond to the “OFF” and “ON” states of the optical or electrical inputs, respectively. **Figure 5a–c** illustrate the output currents for the AND, OR, and NIMP operations, respectively, where an output current below 100 nA is defined as “0” and a current exceeding 100 nA is defined as “1”.

The “AND” logic operation enables hardware-interconnected data communication, ensuring the security of encoding, transmission, and decoding processes. In this context, the ON/OFF state of the light pulse represents the first digit of the digital information, while the ON/OFF state of the  $V_{gs}$  pulse represents the second digit. In a proof-of-concept experiment for data communication, the output currents for the signal units 00, 01, 10,

and 11 are 2 nA (denoted as A), 28 nA (denoted as B), 53 nA (denoted as C), and 140 nA (denoted as D), respectively. According to the American Standard Code for Information Interchange (ASCII), each element of the string “Tianjin” is encoded as a combination of four output currents: BBBA, BCCB, BCAB, BCDC, BCCC, BCCB, BCDC. To avoid interference between signal units, electrical erasure of the flash memory is required after each encoding. Finally, the read signal can be decoded based on the optoelectronic characteristics of the hardware device, as illustrated in **Figure 5d**.

## 2.5. Opto-Electronic Neural Network for Image Classification

To evaluate the learning capability of opto-electronic synapse devices, we constructed an opto-electronic neural network (ONN) based on a three-layer perceptron architecture. The ONN consists of an input layer (784 neurons), a hidden layer (100 neurons), and an output layer (five neurons), which is used for the perception, training, and recognition of color vision test plates, as shown in **Figure 6a**. The images were preprocessed and rescaled to 28 × 28 pixels to match the 784 input neurons; the neural

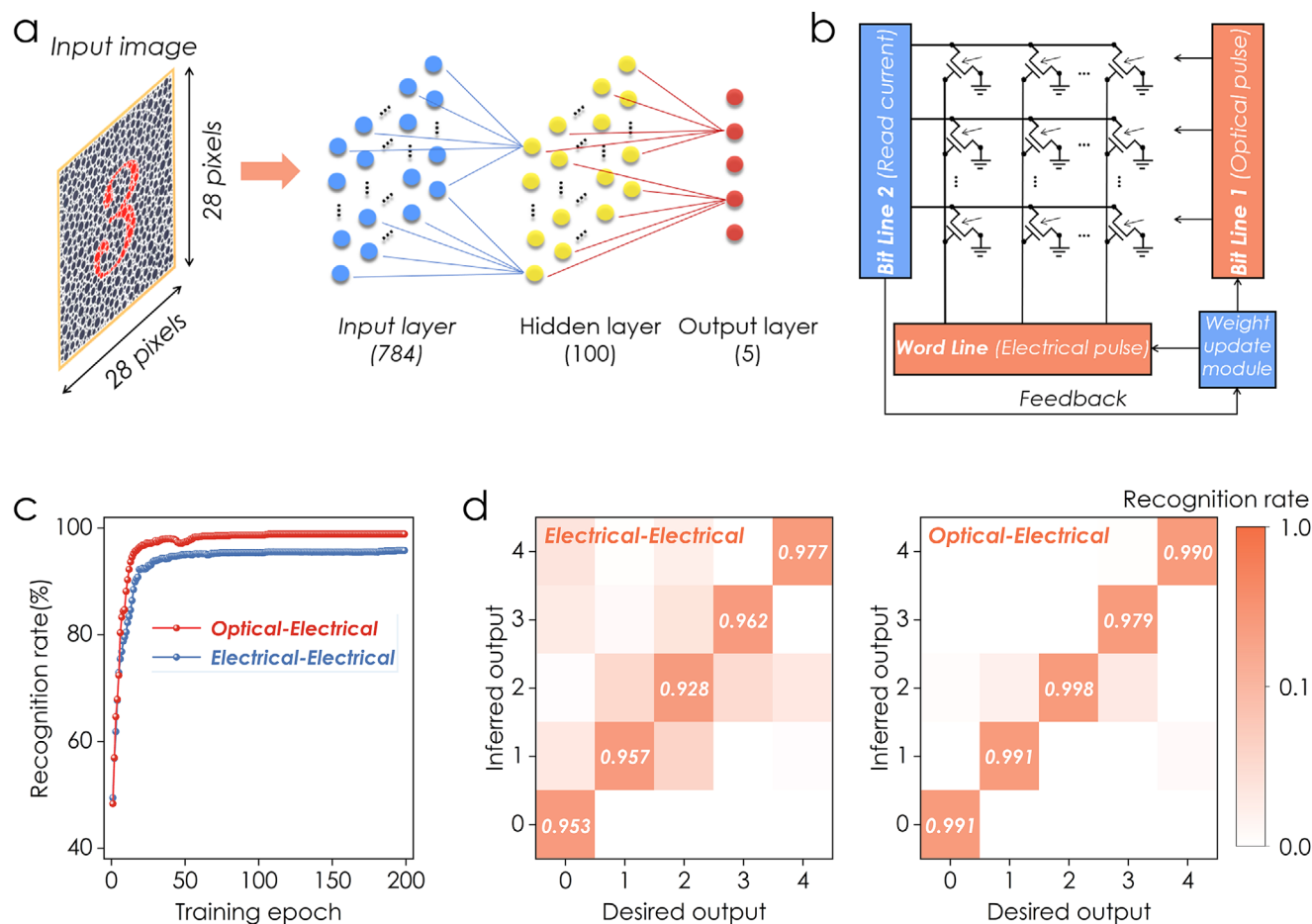


**Figure 6.** Hardware simulation of the ONN. a) Schematic diagram of a three-layer ONN consisting of 784 input neurons, 100 hidden neurons, and five output neurons. b) Schematic diagram of the hardware circuit, including the opto-electronic synapse array and peripheral circuits. c) Recognition rates as a function of optical-electrical and electrical-electrical training epochs. d) Confusion matrix showing the comparison between expected and predicted values after 200 optical-electrical and electrical-electrical training epochs.

network classifies images into five categories: “animal” (labeled as “0”), “graphic” (labeled as “1”), “number” (labeled as “2”), “English word” (labeled as “3”), and “Chinese word” (labeled as “4”), corresponding to the five output neurons.

The training process of the ONN follows the backpropagation algorithm, where 10 000 initial samples and their weighted sums are fed into the input and hidden layers. After activation by the log-sigmoid function, the classification result is passed to the output layer. Figure 6b shows the simulated circuit diagram, including the opto-electronic synapse array and peripheral circuits. The weight update module operates based on the inner product of the input signal vector and the synapse matrix, updating synaptic weights and providing feedback to the synapse array. To evaluate the potential of OEFGT with multilevel storage states, 1000 test images were used for pattern recognition with both electrical and optoelectronic synapses.

The test results are presented in Figure 6c. The electrical synapses, using electrical LTP and electrical LTD synaptic weights to perform electrical-electrical training, achieved a recognition rate of 95.8% after 200 training epochs. The optoelectronic synapses, employing optical LTP and electrical LTD synaptic

weights for optical-electrical training, exhibited a higher recognition rate of 98.8%. After 200 training epochs, the confusion matrix generated from the classification results is shown in Figure 6d. This matrix demonstrates that the ONN achieves more accurate image classification in the optical-electrical mode, covering categories from “0” to “4”. Clearly, optoelectronic synapses, with low energy consumption and multiple conductance states, present a promising approach for the development of efficient neuromorphic computing systems.

### 3. Conclusion

In summary, we have successfully fabricated an opto-electronic synapse device based on  $\text{ReS}_2/\text{h-BN}/\text{Graphene}$  van der Waals heterostructure, achieving high-precision multibit synaptic weights (1024 levels, 10-bit resolution) and ultra-low energy consumption (500 fJ/spike) in optical mode. Benefitting from the superior storage capability, the synapse device successfully simulated optoelectronic modulated synaptic plasticity. Furthermore, through the optoelectronic coupling at the dual-input terminals, the device achieved biomimetic associative learning,

reconfigurable logic functions, and reliable data communication, confirming its in-memory computing capabilities. Finally, based on the LTP/LTD characteristics under optical erasing and electrical programming processes, we simulated an efficient ONN system for pattern recognition of color vision test plates, achieving high recognition accuracy. This work highlights the potential of OEFGT-based optoelectronic synapses with unprecedented optical synaptic weights, paving the way for energy-efficient and high-accuracy neuromorphic computing.

## 4. Experimental Section

**Device Fabrication:** Graphene, h-BN, and ReS<sub>2</sub> flakes were sequentially transferred onto a 285 nm SiO<sub>2</sub>/Si substrate through mechanical exfoliation. The patterning of the electrodes was achieved by electron beam lithography with positive photoresist. After exposure and development, 10/30 nm Cr/Au electrodes were deposited via electron beam evaporation. Finally, the device was completed after a standard lift-off process.

**Device Characterization:** Raman spectra were obtained using a commercial Raman spectrometer (Renishaw, Inc.) with a 532 nm laser source. AFM images were taken with a Bruker Dimension. Electrical and optical tests were conducted at room temperature and in the dark on a Metatest E2 fiber-coupled photoelectric test probe station. The electrical pulses for gate input were provided by a Keithley 2450 single-channel system digital source meter, while the optical pulses received by the channel were generated by a mLaser series light source.

## Supporting Information

Supporting Information is available from the Wiley Online Library or from the author.

## Acknowledgements

Z.Y. and S.H. contributed equally to this work. This study was supported by the open research of Songshan Lake Materials Laboratory (Grant No. 2023SLABFK07), the National Science Foundation of China (Grant Nos. 62304151, 62204170, 62474124, 52125205, 52250398, 52192614 and 52203307), the Natural Science Foundation of Tianjin (Grant No. 24JCQNJC00520), the China Postdoctoral Science Foundation (No. 2023M742585), the State Key Laboratory of Fluid Power and Mechatronic Systems under Grant (No. GZKF-202327).

## Conflict of Interest

The authors declare no conflict of interest.

## Data Availability Statement

The data that support the findings of this study are available from the corresponding author upon reasonable request.

## Keywords

high-precision multibit weights, opto-electronic floating-gate transistors, opto-electronic neural network, opto-electronic synapse, ReS<sub>2</sub>/h-BN/Graphene vdW heterostructure

Received: April 10, 2025

Revised: June 2, 2025

Published online:

- [1] X. Han, J. Tao, Y. G. Liang, F. Guo, Z. S. Xu, W. Q. Wu, J. H. Tong, M. X. Chen, C. F. Pan, J. H. Hao, *Nat. Commun.* **2024**, *15*, 10.
- [2] C. S. Yang, D. S. Shang, N. Liu, E. J. Fuller, S. Agrawal, A. A. Talin, Y. Q. Li, B. G. Shen, Y. Sun, *Adv. Funct. Mater.* **2018**, *28*, 10.
- [3] C. K. Machens, *Science* **2012**, *338*, 1156.
- [4] P. A. Merolla, J. V. Arthur, R. Alvarez-Icaza, A. S. Cassidy, J. Sawada, F. Akopyan, B. L. Jackson, N. Imam, C. Guo, Y. Nakamura, B. Brezzo, I. Vo, S. K. Esser, R. Appuswamy, B. Taba, A. Amir, M. D. Flickner, W. P. Risk, R. Manohar, D. S. Modha, *Science* **2014**, *345*, 668.
- [5] M. A. Zidan, J. P. Strachan, W. D. Lu, *Nat. Electron.* **2018**, *1*, 22.
- [6] Y. Chai, *Nature* **2020**, *579*, 32.
- [7] C. J. Wan, L. Q. Zhu, Y. H. Liu, P. Feng, Z. P. Liu, H. L. Cao, P. Xiao, Y. Shi, Q. Wan, *Adv. Mater.* **2016**, *28*, 3557.
- [8] Z. Q. Wang, T. Zeng, Y. Y. Ren, Y. Lin, H. Y. Xu, X. N. Zhao, Y. C. Liu, D. Ielmini, *Nat. Commun.* **2020**, *11*, 10.
- [9] S. Zhang, K. X. Guo, L. Sun, Y. Ni, L. Liu, W. L. Xu, L. Yang, W. T. Xu, *Adv. Mater.* **2021**, *33*, 9.
- [10] S. Y. Sun, T. Zhang, S. Q. Jin, X. H. Pan, J. G. Lu, Z. Z. Ye, B. Lu, *Adv. Funct. Mater.* **2024**, *34*, 10.
- [11] R. Q. Yang, Y. Wang, S. Q. Li, D. A. Hu, Q. J. Chen, F. Zhuge, Z. Z. Ye, X. D. Pi, J. G. Lu, *Adv. Funct. Mater.* **2024**, *34*, 9.
- [12] J. Kim, S. Song, J. M. Lee, S. Nam, J. Kim, D. Hwang, S. K. Park, Y. H. Kim, *Small* **2023**, *19*, 10.
- [13] X. X. Liu, S. Y. Wang, Z. Y. Di, H. Q. Wu, C. S. Liu, P. Zhou, *Adv. Sci.* **2023**, *10*, 9.
- [14] J. L. Meng, T. Y. Wang, L. Chen, Q. Q. Sun, H. Zhu, L. Ji, S. J. Ding, W. Z. Bao, P. Zhou, D. W. Zhang, *Nano Energy* **2021**, *83*, 11.
- [15] Y. L. Sun, M. J. Li, Y. T. Ding, H. P. Wang, H. Wang, Z. M. Chen, D. Xie, *InfoMat* **2022**, *4*, 12.
- [16] T. P. A. Bach, S. Cho, H. Kim, D. A. Nguyen, H. Im, *ACS Nano* **2024**, *18*, 4131.
- [17] C. Li, X. Chen, Z. R. Zhang, X. S. Wu, T. Z. Yu, R. T. Bie, D. L. Yang, Y. G. Yao, Z. R. Wang, L. F. Sun, *Nano Lett.* **2024**, *24*, 15025.
- [18] H. Y. Lu, Y. Wang, X. C. Han, J. Liu, *ACS Nano* **2024**, *18*, 23403.
- [19] E. X. Wu, Y. Xie, S. J. Wang, D. H. Zhang, X. D. Hu, J. Liu, *Nanoscale* **2020**, *12*, 18800.
- [20] Y. Liu, N. O. Weiss, X. D. Duan, H. C. Cheng, Y. Huang, X. F. Duan, *Nat. Rev. Mater.* **2016**, *1*, 17.
- [21] K. S. Novoselov, A. Mishchenko, A. Carvalho, A. H. C. Neto, *Science* **2016**, *353*, 7.
- [22] A. K. Geim, I. V. Grigorieva, *Nature* **2013**, *499*, 419.
- [23] S. D. Huo, H. Z. Qu, F. Y. Meng, Z. Zhang, Z. Y. Yang, S. L. Zhang, X. D. Hu, E. X. Wu, *Nano Lett.* **2024**, *24*, 11937.
- [24] L. K. Ma, Y. L. Wang, Y. Liu, *Chem. Rev.* **2024**, *124*, 2583.
- [25] D. Kireev, S. Liu, H. Jin, T. P. Xiao, C. H. Bennett, D. Akinwande, J. A. C. Incorvia, *Nat. Commun.* **2022**, *13*, 4386.
- [26] M. Rahman, K. Davey, S. Z. Qiao, *Adv. Funct. Mater.* **2017**, *27*, 21.
- [27] S. Tongay, H. Sahin, C. Ko, A. Luce, W. Fan, K. Liu, J. Zhou, Y. S. Huang, C. H. Ho, J. Y. Yan, D. F. Ogletree, S. Aloni, J. Ji, S. S. Li, J. B. Li, F. M. Peeters, J. Q. Wu, *Nat. Commun.* **2014**, *5*, 6.
- [28] Y. L. He, S. Nie, R. Liu, S. S. Jiang, Y. Shi, Q. Wan, *Adv. Mater.* **2019**, *31*, 8.
- [29] C. Zhu, *Light: Sci. Appl.* **2022**, *11*, 337.
- [30] J. Bak, S. Kim, K. Park, J. Yoon, M. Yang, U. J. Kim, H. Hosono, J. Park, B. You, O. Kwon, B. Cho, S.-W. Park, M. G. Hahm, M. Lee, *Acs Appl. Mater. Interfaces* **2023**, *15*, 39539.
- [31] H. Guo, J. Guo, Y. Wang, H. Wang, S. Cheng, Z. Wang, Q. Miao, X. Xu, *ACS Appl. Mater. Interfaces* **2024**, *16*, 66948.
- [32] E. Lee, J. Kim, J. Park, J. Hwang, H. Jang, K. Cho, W. Choi, *ACS Appl. Mater. Interfaces* **2023**, *15*, 15839.
- [33] C. Liu, J. Pan, Q. Yuan, C. Zhu, J. Liu, F. Ge, J. Zhu, H. Xie, D. Zhou, Z. Zhang, P. Zhao, B. Tian, W. Huang, L. Wang, *Adv. Mater.* **2024**, *36*, 2305580.
- [34] R. D. Nikam, K. G. Rajput, H. Hwang, *Small* **2021**, *17*, 2006760.

- [35] M.-K. Song, H. Lee, J. H. Yoon, Y.-W. Song, S. D. Namgung, T. Sung, Y.-S. Lee, J.-S. Lee, K. T. Nam, J.-Y. Kwon, *J. Mater. Sci. Technol.* **2022**, 119, 150.
- [36] Y. Sun, N. He, Y. Wang, Q. Yuan, D. Wen, *Nano Energy* **2022**, 98, 107252.
- [37] C. Zhang, J. Ning, W. Lu, B. Wang, X. Cui, X. Zhu, X. Shen, X. Feng, Y. Wang, D. Wang, X. Wang, J. Zhang, Y. Hao, *Small* **2023**, 19, 2370263.
- [38] Y. Zhou, Y. Wang, F. Zhuge, J. Guo, S. Ma, J. Wang, Z. Tang, Y. Li, X. Miao, Y. He, Y. Chai, *Adv. Mater.* **2022**, 34, 2107754.
- [39] M. Saponati, M. Vinck, *Nat. Commun.* **2023**, 14, 13.
- [40] T. Boynazarov, J. Lee, H. Lee, S. Lee, H. Chung, D. H. Ryu, H. Abbas, T. Choi, *J. Mater. Sci. Technol.* **2025**, 227, 164.
- [41] R. A. John, F. C. Liu, N. A. Chien, M. R. Kulkarni, C. Zhu, Q. D. Fu, A. Basu, Z. Liu, N. Mathews, *Adv. Mater.* **2018**, 30, 9.